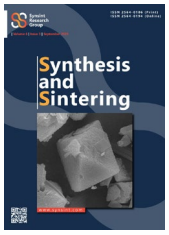
Available online at www.synsint.com

Synthesis and Sintering

ISSN 2564-0186 (Print), **ISSN** 2564-0194 (Online)



Research article

Rational design of a hierarchical g-C_3N_4/copper-MOF/Fe_3O_4 ternary composite for potential photocatalytic applications

Seyed Ali Zargar, Ali Moeini, Adrine Malek Khachatourian *, Mohammadamin Aghdamshahriar, Seyedamirabbas Estahbanati

Department of Materials Science and Engineering, Sharif University of Technology, Tehran, Iran

ABSTRACT

Photocatalysis is an eco-friendly approach for water remediation. Solar radiation can serve as a natural source of visible light for photocatalytic processes, making visible-light-driven photocatalysis a promising approach for practical environmental applications. Along with visible light absorption and a highly active surface, the primary requirements of photocatalysts, facile separation for reuse is a key feature for photocatalyst development. Herein, a hierarchically separable ternary composite of g-C_3N_4/Cu-BTC MOF/Fe_3O_4, denoted CNMF, was fabricated as a potential photocatalyst material. The g-C_3N_4 and Fe_3O_4 were obtained via thermal polymerization and co-precipitation, respectively. Finally, the copper metal-organic framework (Cu-MOF) was synthesized in situ using a solvothermal method in the presence of g-C_3N_4 and Fe_3O_4. The morphological, structural, optical, elemental, and magnetic properties of the synthesized materials were investigated. Morphological studies showed a hierarchical architecture in which faceted Cu-MOF crystallites and Fe_3O_4 nanoparticles were integrated with layered g-C_3N_4. The band gap energy of CNMF was calculated as 2.94 eV. Thus, it benefits from the high visible absorption of g-C_3N_4, high redox capacity of Cu-MOF, and easy recyclability and reusability of Fe_3O_4. CNMF exhibited superparamagnetic behavior with a saturation magnetization of approximately 2.19 emu g^{-1}. The findings of the study confirm the potential of CNMF as a magnetically recoverable candidate for photocatalytic applications.

© 2026 The author(s) retain the copyright and full publishing rights.

KEYWORDS

Photocatalysis
Metal-organic framework
Hierarchical heterostructure
Recoverable photocatalyst
Bandgap tuning
Electronic modification

OPEN ACCESS

1. Introduction

The need for more accessible fresh water has become a major issue due to the growing population. Additionally, rising levels of contaminated water result from the rapid pace of industrialization and urbanization [1]. To address the shortage of fresh water, various water remediation techniques, such as reverse osmosis [2], membrane filtration [3], electrodialysis [4], capacitive deionization [5], etc., have been introduced. However, these techniques face limitations, including the generation of secondary pollution, low efficiency, and environmental issues. Photocatalysis has been positioned as an efficient method for the degradation of pollutants in water, hydrogen generation, water splitting, and related applications [6, 7]. This method is of great interest due to its environmental friendliness and high energy efficiency [8]. Photocatalysis is a process that can remove water pollutants by directly converting light into energetic particles. Semiconductor photocatalysts are the primary materials used in this application due to their appropriate band gap and ability to generate photogenerated species. Photocatalyst materials have two major characteristics that make them suitable for photocatalysis: band gap energy and specific surface area. The former determines the portion of the solar spectrum that can be absorbed and the redox potential of the photogenerated charge carriers,

* Corresponding author. *E-mail address:* khachatourian@sharif.edu (A.M. Khachatourian)
Received 2 September 2026; Received in revised form 29 September 2026; Accepted 29 September 2026.
This is an open access article under the CC BY license (https://creativecommons.org/licenses/by/4.0/). Published by Synsint Research Group.
https://doi.org/10.53063/synsint.2026.63370

while the latter influences the adsorption of pollutant molecules and the occurrence of photocatalytic reactions [9, 10].

Among various adopted semiconductors in the field, the metal-free graphitic carbonitride (g-C_3N_4) semiconductor has garnered significant attention due to a favorable band gap energy (≈ 2.7 eV) that leads to high adsorption in the visible light region [11, 12]. It also possesses excellent chemical stability, biocompatibility, a simple synthesis process, and cost-effectiveness [13]. Nevertheless, pure g-C_3N_4 suffers from intrinsic challenges, such as electron-hole pair recombination and a low surface area, which severely limit the number of active sites and reactant adsorption [14]. Therefore, combining g-C_3N_4 with a second component with a large surface area and well-aligned band edges is expected to be an effective approach to address both issues simultaneously.

Metal-organic frameworks (MOFs) have emerged as outstanding candidates for solar light harvesting and photocatalytic applications owing to their exceptional structural characteristics, including stability, high specific surface area, and readily tunable porous structures [15]. MOFs are a family of porous hybrid crystalline materials made up of organic ligands acting as linkers and an array of metal ions that form a three-dimensional structure resembling a cage [16]. Copper-based MOFs (Cu-MOFs) are of particular interest to researchers as photocatalysts because copper can undergo numerous transformations and is widely recognized as an effective catalyst. In the crystalline structure of Cu-MOFs, Cu^{2+} nodes act as catalytic sites linked via an organic linker [17]. Cu-MOFs benefit from excellent structural stability, non-toxicity, and the availability of copper in nature [18]. For example, Zhu et al. [19] prepared a Cu-NTC MOF consisting of copper as the metal node and 1,4,5,8-naphthalene tetracarboxylic acid as the ligand, achieving a high photodegradation efficiency of 84.5% toward the tetracycline pollutant. However, the band gap energy of Cu-MOF is quite high, limiting its application as a standalone photocatalyst. As reported in the literature, g-C_3N_4/MOF binary composites can form strong heterojunctions, making them suitable for photocatalytic applications [20, 21]. Thus, the g-C_3N_4/Cu-MOF heterojunction can surpass the photocatalytic performance of the individual components. In this case, the organic linker molecules in the MOF can bond with the triazine rings of the g-C_3N_4 framework to form π–π interactions [22].

A key factor in evaluating the practicability of the materials for photocatalytic applications, specifically photocatalytic pollutant removal, is the material's recovery potential. In this context, magnetic materials can play a role [23]. One common iron oxide with magnetic recovery properties is magnetite (Fe_3O_4) [24]. It shows strong superparamagnetic behavior, enabling simple magnetic separation of the catalyst from treated water and making the system reusable. Moreover, Fe_3O_4 benefits from a relatively low band gap energy (≈ 2.1 eV), contributing to visible-light absorption, environmental friendliness, and biocompatibility. Despite all these advantages, the tendency of bare Fe_3O_4 nanoparticles (NPs) to aggregate through magnetic dipole-dipole interactions can reduce their efficiency. To overcome this limitation, combining Fe_3O_4 with other catalysts can be a practical approach. This strategy cannot only prevent NP agglomeration through surface bonding but also enhance the resulting photocatalytic activity [25].

Herein, a hierarchical g-C_3N_4/Cu-MOF/Fe_3O_4 ternary composite has been constructed to serve as a potent candidate for photocatalytic applications. Despite previous investigations of g-C_3N_4/MOF hybrids and magnetic photocatalysts, the simultaneous integration of g-C_3N_4, Cu-MOF, and Fe_3O_4 into a hierarchical ternary architecture remains a promising approach that warrants further investigation, particularly regarding the complementary roles of light absorption, catalytic-site availability, and magnetic separation within a single material. In this vein, g-C_3N_4 with a fluffy structure was prepared via a simple thermal polymerization approach. Next, Fe_3O_4 NPs were fabricated via co-precipitation. Finally, we used a simple solvothermal approach to grow Cu-MOF octahedra in situ on the Fe_3O_4/g-C_3N_4 binary solution. The assembly of Cu-MOF on g-C_3N_4 may be facilitated by interfacial interactions between the aromatic framework of the MOF linker and the conjugated structure of g-C_3N_4. The integration of g-C_3N_4, Cu-MOF, and Fe_3O_4 offers a promising strategy to combine efficient light harvesting, favorable redox properties, and practical recoverability in a composite material. The as-prepared ternary composite displayed a band gap energy of 2.94 eV, suggesting its potential for light-driven photocatalytic applications. In this system, the g-C_3N_4 component can serve as the major absorber of visible light. Meanwhile, the Cu-MOF can provide numerous catalytic sites due to a high theoretical surface area. Their interface can potentially facilitate charge transfer. Compared with binary g-C_3N_4/MOF systems, the incorporation of Fe_3O_4 introduces an additional magnetic functionality that may facilitate catalyst recovery, whereas the combination of g-C_3N_4 and Cu-MOF is intended to couple semiconductor-based light harvesting with the accessible catalytic sites of the MOF. Thus, the ternary design aims to integrate photocatalytic functionality and magnetic recoverability while potentially improving interfacial charge-transfer behavior. Therefore, it is expected that CNMF is a potentially effective and reusable material for visible-light-driven applications.

2. Experimental procedure

2.1. Materials

Urea ($CO(NH_2)_2$, ≥99%), Ferrous chloride tetrahydrate ($FeCl_2.4H_2O$, ≥99%), ferric chloride hexahydrate ($FeCl_3.6H_2O$, ≥99%), hydrochloric acid (HCl, 37%), ammonium hydroxide (NH_4OH, 25%), copper (II) nitrate trihydrate ($Cu(NO_3)_2.3H_2O$, ≥99%), and 1,3,5-benzenetricarboxylic acid (H3BTC) precursors were purchased from Merck Company. All reagents were purchased as analytical grade to use without purification. Dimethylformamide (DMF), absolute ethanol, and deionized (DI) water were obtained from a local supplier.

2.2. Synthesis of bulk g-C_3N_4

The bulk g-C_3N_4 powder was synthesized via a simple thermal heating process, as reported in our previous study [8]. For this purpose, 20 g of urea, as the main precursor, was placed in a crucible and heated at 500 °C for 2 h (heating rate: 2 °C/min). After cooling, the fluffy yellowish g-C_3N_4 was collected. The schematic of the synthesis procedure is shown in Fig. 1.

2.3. Preparation of Fe_3O_4 nanoparticles

According to our previous study, a facile co-precipitation method has been incorporated for the magnetite NPs fabrication [26], as displayed in Fig. 2. In this vein, 0.3976 g of $FeCl_2.4H_2O$ precursor was added to 5 ml of 2 M HCl, while 1.0813 g of $FeCl_3.6H_2O$ was dissolved in 20 ml of 2 M HCl. Choosing HCl rather than DI water facilitates the

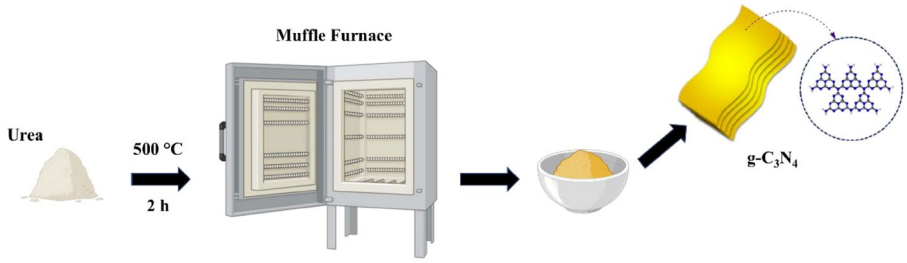


Fig. 1. Schematic of the bulk g-C_3N_4 synthesis procedure.

formation of NPs by preventing the precipitation of Fe(II) and Fe(III) hydroxides. After blending, the solutions were mixed to obtain the synthesis solution. The resulting solution was stirred (600 rpm) at 70 °C under a continuous N_2 gas purge for 30 min. To make the pH basic, 35 ml of a 25% NH_4OH solution was added. The obtained black precipitate was collected using an external magnet and washed with DI water in several steps to remove impurities and reach a neutral pH. Finally, the washed product was vacuum-dried at 60 °C for 24 hours.

2.4. Synthesis of Cu-MOF

Cu-MOF synthesis was performed by a simple solvothermal method, as depicted in Fig. 3. The $Cu(NO_3)_2.3H_2O$ salt served as the source of copper metal ions, while H3BTC was used as the organic linker. The weight ratio of copper to H3BTC in the synthesis procedure was 1.09:1. First, 0.4 g of H3BTC ligand was dissolved in a mixture of ethanol, DI water, and DMF with a 1:1:1 ratio and stirred until homogeneous. Next, 0.436 g of $Cu(NO_3)_2.3H_2O$ was added to the solution, which was then stirred at RT to obtain a uniform solution. The achieved solution was transferred to a Teflon-lined autoclave (capacity: 60 ml) and was heated at 125 °C for 22 h [17]. Subsequently, it naturally cooled to ambient temperature. The solid precipitate was collected, washed with DI water and ethanol, transferred into a vacuum oven, and dried at 60 °C, yielding a bluish Cu-MOF powder.

2.5. Fabrication of g-C_3N_4/Cu-MOF/Fe_3O_4 ternary composite

The g-C_3N_4/Cu-MOF/Fe_3O_4 nanocomposite was fabricated by in situ synthesis of Cu-MOF in the presence of Fe_3O_4 NPs and bulk g-C_3N_4, using a solvothermal technique. In this regard, $Cu(NO_3)_2.3H_2O$ salt precursor and g-C_3N_4 powder were dispersed in 20 ml of DI water, while H3BTC was dispersed in 15 ml of ethanol under constant stirring. After dispersion, the solutions were mixed. In the next step, the Fe_3O_4 powder was added to the above solution and subjected to ultrasonic homogenization. For in situ Cu-MOF formation, the final mixture was transferred to a Teflon chamber and heated in an autoclave at 120 °C for 12 h. The resulting powder was washed several times with DI water and ethanol until the solution reached neutral pH. The precipitate was collected and freeze-dried (Tajhizat Sazan Pishtaz company, F-5 V model) to obtain the g-C_3N_4/Cu-MOF/Fe_3O_4 powder. The obtained powder was labeled as CNMF. The whole CNMF synthesis procedure is illustrated in Fig. 4.

2.6. Materials characterization

The crystallinity and phase formation were evaluated by recording X-ray diffraction (XRD) patterns of powder samples using a PANalytical X'Pert PRO MPD instrument at an operating voltage of 40 kV. CuKα radiation with a wavelength of λ=1.5406 Å was used in this measurement. The composition and properties of structural and surface groups were ascertained by Fourier transform infrared spectroscopy (FTIR) using a Perkin-Elmer Spectrum apparatus in the wavenumber range of 450–4000 cm^{-1}. The ultraviolet–visible spectrophotometer (UV-vis; JENWAY 6705: 200–900 nm wavelength range) was used to assess the optical properties of the as-synthesized materials and their light-absorbing capacity. Microstructural examination and elemental analysis of the samples were performed using a field-emission scanning electron microscope (FESEM, MIRA3 LMU model, TESCAN company, accelerating voltage 15 kV), equipped with an energy-

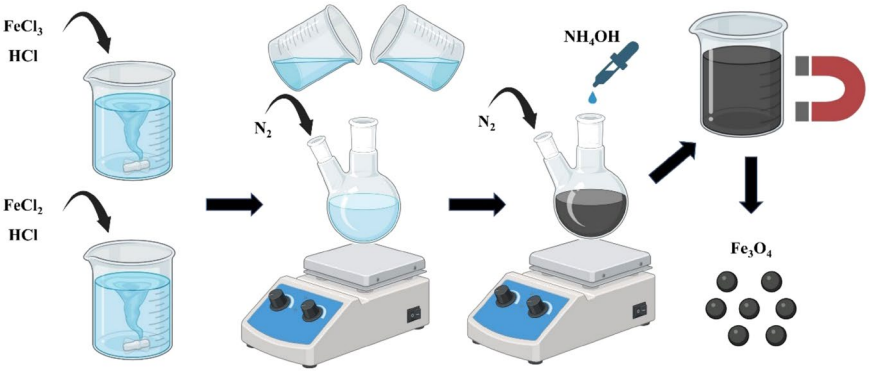


Fig. 2. Schematic of the Fe_3O_4 NPs synthesis process.

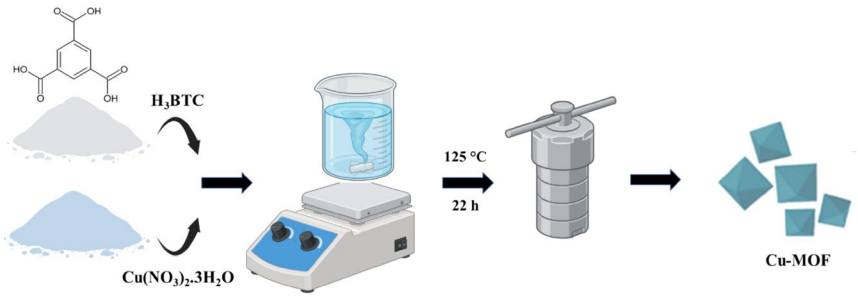


Fig. 3. A schematic illustration of the Cu-MOF fabrication step.

dispersive X-ray spectrometer (EDX). To measure the magnetic properties and magnetization curves of the samples, a vibrating sample magnetometer (VSM) manufactured by MDK was used in a magnetic field of up to 15 kOe.

3. Results and discussion

3.1. Structural studies

To evaluate the quality of the prepared materials, various characterization techniques were employed for structural, microstructural, optical, and magnetic studies.

XRD analysis was used to characterize the phase and evaluate the crystallinity of the samples. Fig. 5a shows the XRD patterns of the synthesized powders. The peaks observed at 2θ angles of 30.1, 35.6, 43.1, 53.4, 57.2, 62.9, and 74.3 are corresponding to the (220), (311), (400), (422), (511), (440), (533) crystal planes of the ferrite structure (JCPDS No. 96–900-2329), respectively, indicating the formation of the inverse spinel structure of the Fe_3O_4 nanoparticles [26]. The red curve assigned to the bulk g-C_3N_4 structure demonstrates a peak at 12.3 ° that is ascribed to the interplanar tri-s-triazine units, while the other peak at 26.9 °, related to the (002) crystal plane, is attributed to the conjugated aromatic network [8]. Regarding the XRD pattern of the Cu-MOF powder, the diffraction peaks appeared at 2θ angles of 6.7, 9.6, 11.6, 13.5, 14.8, 16.6, 17.7, 19.2, 20.4, 21.5, 24.3, 26.1, 27.8, and 29.4 degrees are related to the (200), (220), (222), (400), (331), (422), (511), (440), (600), (620), (551), (731), (822), and (751) crystallographic planes, respectively. The pattern is in good agreement with the Cu-MOF structure, according to the JCPDS card No. 00-062-1183, and shows an FCC structure belonging to space group $Fm\bar{3}m$. In addition, due to the high temperature during the synthesis procedure, some low-intensity peaks appear in the 37 ° to 42 ° range, attributed to copper oxides [17].

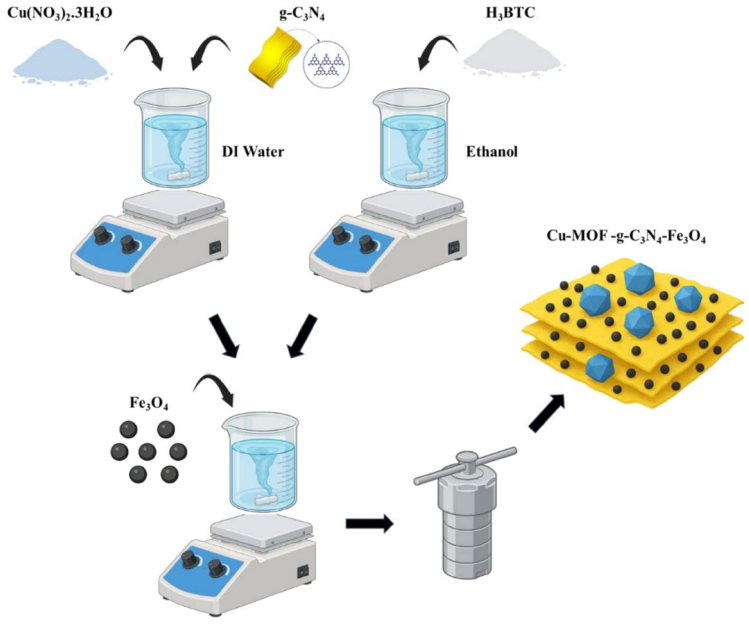


Fig. 4. Schematic illustration of the g-C_3N_4/Cu-MOF/Fe_3O_4 composite preparation process.

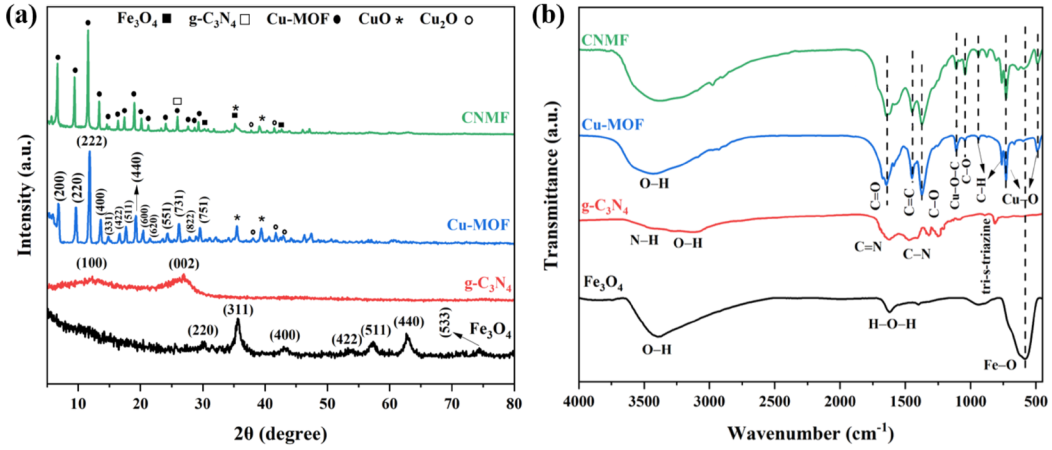


Fig. 5. a) XRD patterns of the synthesized powders and b) FTIR spectra of the as-prepared samples.

In the diffraction pattern of the CNMF ternary composite, characteristic peaks related to the components of the composite, including g-C_3N_4, Fe_3O_4, and Cu-MOF, were identified. This observation can serve as strong evidence of a successful composition process. Moreover, the characteristic diffraction peaks shifted toward lower 2θ values, indicating an increase in the interplanar spacing (d), a sign of lattice expansion. This may have arisen from tensile strain in the framework, owing to a lattice mismatch between components [27]. This peak shift confirms the formation of a heterojunction with an intimate interface. The molecular structure and surface bonds of the samples were evaluated using FTIR. As depicted in Fig. 5b, the FTIR spectrum of the ferrite NPs consists of a broad band around 3400 cm^{-1} and a weak dip at ≈ 1621 cm^{-1} that derives from O–H bond stretching of surface-adsorbed water and hydroxyl groups on the magnetite, as well as a strong band centered around 582 cm^{-1}, representing the intrinsic vibration of the Fe–O bond in the tetrahedral sites [28]. In the bulk g-C_3N_4 spectrum (Fig. 5b), a wide band ranging from 3640 cm^{-1} to 2950 cm^{-1} appears, which comes from N–H stretching of residual amino groups plus adsorbed water molecules. A cluster of bands in the ~1200–1650 cm^{-1} region is attributed to the stretching of aromatic CN heterocycle within the tri-s-triazine units [29]. The last band at 810 cm^{-1} is the breathing mode of the tri-s-triazine (heptazine) ring and is the fingerprint peak of the g-C_3N_4 network [8]. There are multiple bands in the FTIR spectra of the Cu-BTC sample, including metal center species, organic linker molecules, and their interactions, as shown in Fig. 5b (blue curve). Apart from the hydroxyl characteristic peak at 3431 cm^{-1}, two sharp bands at 1645 cm^{-1} and 1373 cm^{-1} are correlated to carboxylate group stretching, while the peak located at 1449 cm^{-1} is assigned to the aromatic C=C ring stretching. A pair of peaks at 938 cm^{-1} and 759 cm^{-1} is attributed to the out-of-plane aromatic C–H bending. A strong interaction between the metal and the linker appears as a Cu–O–C stretching band at 1108 cm^{-1}. A weak C–O bond-related peak at around 1045 cm^{-1} is derived from an aromatic ring vibration. Additionally, three prominent peaks are displayed in the fingerprint region (below 1000 cm^{-1}), which are ascribed to the Cu–O bond. The source of these peaks at 730 cm^{-1}, 664 cm^{-1}, and 489 cm^{-1} is Cu^{2+}–carboxylate coordination, framework vibration, and out-of-plane BTC vibration, respectively [17]. Finally, the FTIR spectrum of the ternary CNMF composite (green curve, Fig. 5b) exhibits the combined fingerprints of all three constituents, confirming their successful integration. A broad band near 3375 cm^{-1} corresponds to O–H/N–H stretching of adsorbed water and residual amine groups. The band around 1640 cm^{-1} is assigned to C=O of the Cu-BTC framework, while the 1380–1610 cm^{-1} region arises from overlapping aromatic C=C/C=N and symmetric carboxylate (C–O) vibrations of the Cu-MOF and g-C_3N_4. The coexistence of the peaks relevant to the tri-s-triazine of g-C_3N_4 (~806 cm^{-1}), the spinel Fe–O bond (~585 cm^{-1}), as well as the Cu-MOF structure, verifies the intimate coupling of g-C_3N_4, Cu-MOF, and Fe_3O_4 within the hierarchical heterostructure.

3.2. Microstructural studies

To study the microstructure of the synthesized materials, FE-SEM and EDS characterization techniques were employed. As depicted in Fig. 6a, the bulk g-C_3N_4 exhibits an irregular structure composed of loosely packed layered stacks. Fig. 6b displays the sponge-like texture of this material with clear pores, which provides a high surface area favorable for anchoring secondary nanoparticles. The Cu-MOF presents faceted polyhedral crystals with sharp edges and smooth crystalline faces (Fig. 6c). This microstructure is indicative of a highly ordered coordination framework, achieved through controlled nucleation conditions. Fe_3O_4 shows typical agglomerated spherical nanoparticles that form huge aggregates (Fig. 6d). The corresponding histogram is displayed in Fig. 6e. The particle size distribution follows a near-Gaussian profile centered on an average diameter of 18.9 nm, confirming the successful synthesis of magnetite in the nanoscale regime, which is essential for imparting magnetic separability to the final composite. As illustrated in the FESEM images of the CNMF ternary composite at multiple magnifications (Figs. 6f & 6h), the composite reveals a hierarchical heterostructure in which the distinct morphological signatures of all three components are simultaneously preserved and intimately interconnected. The magnetite NPs are uniformly decorated on the wrinkled g-C_3N_4 surfaces, while the angular Cu-MOF polyhedra remain embedded within and partially encapsulated by the g-C_3N_4/Fe_3O_4 matrix. This intimate contact between phases indicates strong interfacial interactions that likely facilitate efficient charge-transfer pathways across heterojunctions [8]. The microstructural findings are in line with the peak shift observed in the XRD analysis. As shown in the EDS spectrum of the CNMF

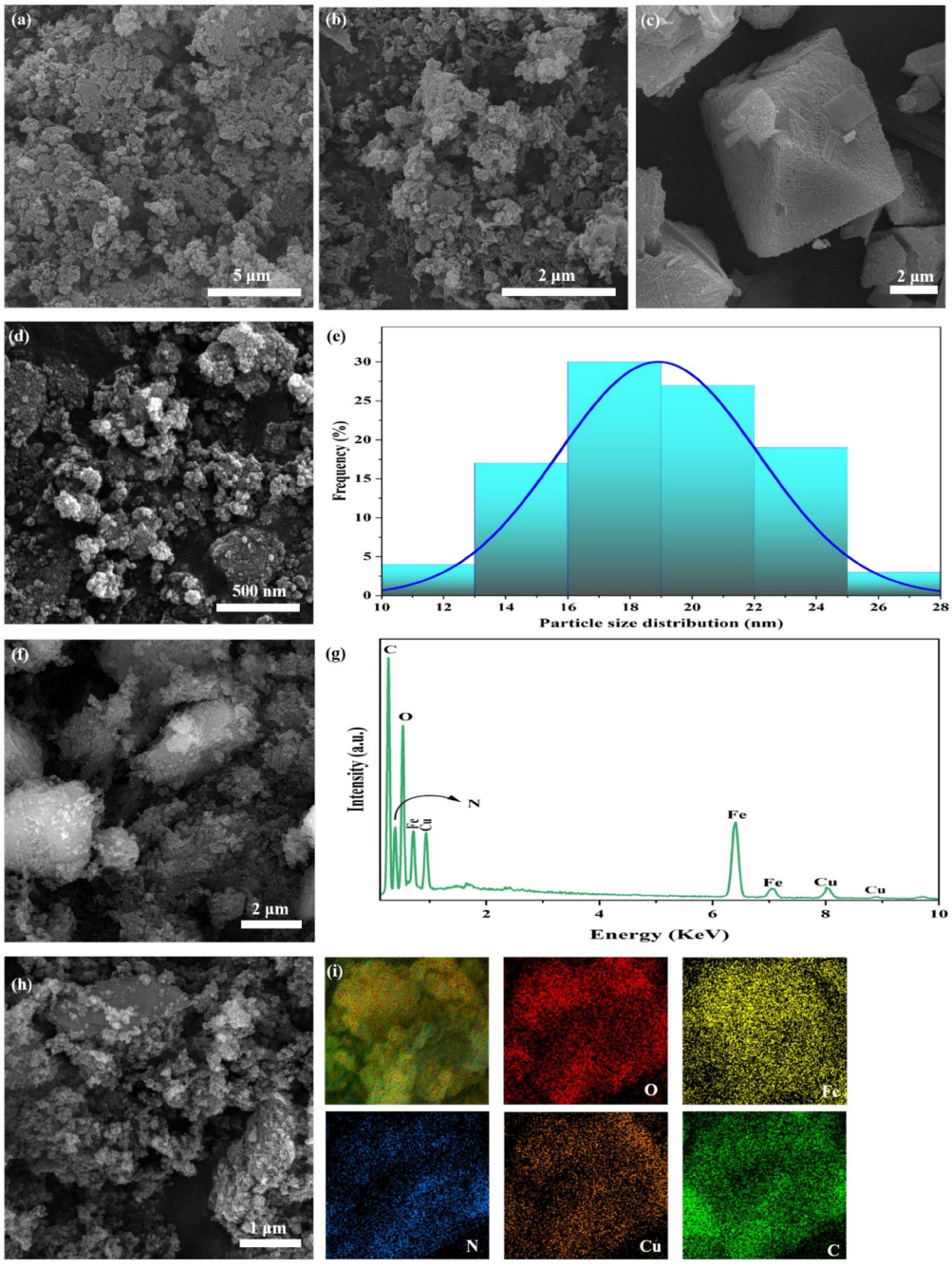


Fig. 6. FE-SEM images of a, b) g-C_3N_4, c) Cu-MOF, d) Fe_3O_4, and f,h) CNMF composite; e) particle size distribution of Fe_3O_4; g) the EDS spectra of the CNMF composite; and i) elemental mappings of the CNMF composite.

sample (Fig. 6g), peaks corresponding to C, O, N, Fe, and Cu elements are observed, confirming the presence of all components in the composite structure. Carbon and oxygen peaks reflect the g-C_3N_4 and MOF organic linkers, while the N signal corresponds to the triazine/heptazine units of g-C_3N_4. Fig. 6i shows the elemental mapping of the composite. The homogeneous distribution of the elements throughout the structure, with no significant phase segregation, further corroborates the structural integration. This uniform elemental dispersion strongly supports the formation of a heterostructure rather than a physical blend.

3.3. Optical studies

The UV-Vis absorption spectra of the components, along with their corresponding Tauc plots, are illustrated in Fig. 7. The absorption curve of g-C_3N_4 (red curve, Fig. 7a) exhibits a strong band around 360 nm, extending into the visible light region. This behavior comes from the

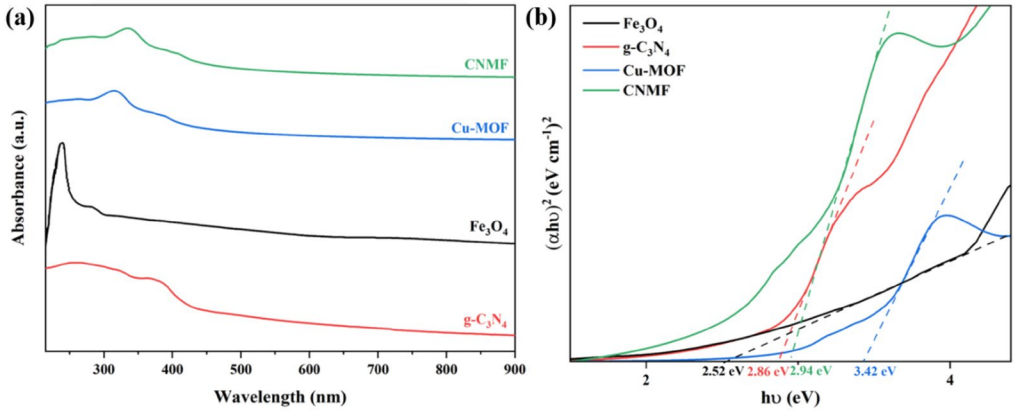


Fig. 7. a) UV–Vis absorption spectra and b) Tauc plots of the as-prepared samples.

π–π* electronic transitions of the aromatic C–N heterocyclic rings and the n–π* transitions associated with the lone pairs of the bridging nitrogen atoms within the heptazine network [8]. As shown in the Fe_3O_4 spectrum, a broad absorption band reflects the narrow band gap and metallic behavior typical of magnetite, consistent with previous findings [26]. The UV-Vis curve of Cu-MOF displays an absorption band in the range of 316 nm to 389 nm, driven by two contributors: π–π* transitions of the aromatic organic linker as well as the charge transition between metal nodes and linker. The peak location indicates that Cu-MOF is highly active in the ultraviolet region and has a wide band gap. The UV-Vis spectrum of CNMF shows a redshift and a greater tendency towards the visible range compared to Cu-MOF. This behavior confirms a synergistic optical response of the ternary system. Herein, the conjugated g-C_3N_4 framework supplies intrinsic visible-light absorption, the Cu-MOF contributes its characteristic charge-transfer transitions, and the Fe_3O_4 nanoparticles impose their broadband absorption across the visible–NIR region. Therefore, it can be concluded that intimate interfacial contact can promote electronic coupling within the hierarchical architecture. This subject can broaden the optical absorption window and enhance the overall light-harvesting capability of CNMF. This behavior is favorable for enhanced photocatalytic activity.

To calculate the band gap energies of the materials, the Kubelka-Munk formula (Eq. 1) was applied [30], and the corresponding Tauc plots are shown in Fig. 7b.

$$\alpha h\nu = A(h\nu - E_g)^n \quad (1)$$

Here, α denotes the absorption coefficient, hν represents the incident photon energy, A is a material-dependent constant, E_g signifies the band gap energy, and n characterizes the type of electronic transition occurring in the semiconductor [31, 32]. The band gap energies of all materials were calculated and reported in Table 1.

The band gap energy of Fe_3O_4 was 2.52 eV. The band gap was calculated to be 2.86 eV for g-C_3N_4, aligning with reported values in the literature [33] and consistent with its visible-light absorption up to ~ 430 nm observed in the UV–Vis spectrum. The E_g of the Cu-MOF was 3.42 eV, indicating the largest band gap among all samples and corroborating predominantly UV activity. The band gap energy of the CNMF ternary composite falls between those of Cu-MOF and g-C_3N_4, a result attributable to the formation of an intimate heterojunction between the components, which leads to strong interfacial electronic interactions and charge redistribution across the interface. This is favorable for enhancing the photocatalyst's light absorption capacity. Consequently, the CNMF specimen simultaneously combines the strong visible-light absorption characteristic of g-C_3N_4 with the photoredox capability of Cu-MOF [16, 34, 35].

3.4. Magnetic studies

The magnetic properties of the synthesized samples were investigated via the vibrating sample magnetometer (VSM) technique. As shown in Fig. 8, the Fe_3O_4 sample exhibits negligible remanence at room temperature, indicating superparamagnetic behavior. This behavior enables rapid response to magnetic excitation and easy dispersion in solution without agglomeration upon removal of the external magnetic field [24]. The g-C_3N_4 and Cu-MOF samples exhibit no saturation magnetization, indicating that these materials lack magnetic properties. The CNMF sample exhibits superparamagnetic properties with a saturation magnetization of about 2.19 emu/g, due to the presence of Fe_3O_4 nanoparticles. Therefore, this sample can be collected in a mixture by applying an external magnetic field (inset of Fig. 8). In contrast to the non-magnetic g-C_3N_4 and Cu-MOF samples, the presence of Fe_3O_4 within the CNMF structure imparts a distinct magnetic response. Given the nanoscale dimensions of the Fe_3O_4 particles and their superparamagnetic behavior, the CNMF sample's magnetization is primarily attributed to the magnetic Fe_3O_4 phase. This characteristic demonstrates that the stabilization of Fe_3O_4 within the composite structure not only preserves the photocatalytic capabilities of the constituent components but also enables magnetic control and recovery of the material. This capability is of great importance in the field of catalysts, making CNMF a suitable photocatalyst candidate for water remediation in real-world applications.

Table 1. Calculated band gap energies of materials.

Material type	E_g (eV)
Fe_3O_4	2.52
g-C_3N_4	2.86
Cu-MOF	3.42
CNMF	2.94

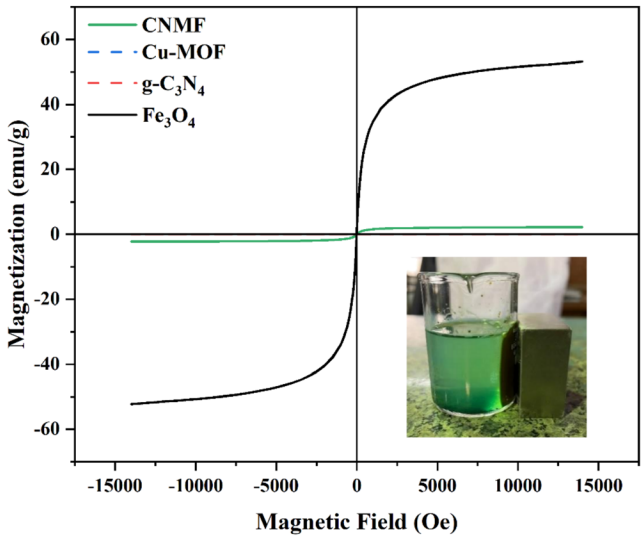


Fig. 8. VSM hysteresis loop at room temperature of Fe_3O_4, g-C_3N_4, Cu-MOF, and CNMF nanocomposites.

4. Conclusions

A hierarchical ternary composite of g-C_3N_4/Fe_3O_4/copper-MOF (CNMF) has been prepared by in situ formation of Cu-BTC MOF on the g-C_3N_4/Fe_3O_4 interface via a simple solvothermal method. The successful composite construction was confirmed by the results of various characterization techniques. The microstructural studies showed that CNMF maintained the fluffy structure of g-C_3N_4, the faceted crystalline structure of the Cu-MOF, and the presence of Fe_3O_4 nanoparticles, confirming the formation of an interconnected hierarchical structure with a uniform distribution of the elements. According to the optical investigations, the band gap energy of CNMF was 2.94 eV, a value that lies between those of the individual components and indicates that the electronic structure has been altered as a result of the composite formation. In the CNMF system, the g-C_3N_4 with a narrow band gap energy functions as the primary absorber of visible light, while the Cu-MOF offers photoredox reactions owing to its high surface area. At the same time, the saturation magnetization of approximately 2.19 emu g^{-1} facilitates facile separation of the composite material with an external magnet. This characteristic is derived from the magnetic properties of Fe_3O_4 nanoparticles. These features suggest that CNMF may be a promising candidate for future photocatalytic applications.

CRediT authorship contribution statement

Seyed Ali Zargar: Investigation, Validation, Conceptualization, Writing – original draft, Visualization.
Ali Moeini: Investigation, Methodology, Validation, Resources, Conceptualization, Writing – original draft.
Adrine Malek Khachatourian: Supervision, Project administration, Methodology, Conceptualization, Resources, Writing – Reviewing & editing.
Mohammadamin Aghdamshahriar: Investigation, Resources.
Seyedamirabbas Estahbanati: Investigation, Resources.

Data availability

The data underlying this article will be shared on reasonable request to the corresponding author.

Declaration of competing interest

The authors have no competing interests to declare that are relevant to the content of this article.

Funding and acknowledgment

No funding was received. The authors would like to acknowledge the Deputy of Research and Technology at Sharif University of Technology for supporting this research. The authors would like to acknowledge Ms. Elham Soroush for her invaluable assistance and support throughout this research.

References

[1] N. Morin-Crini, E. Lichtfouse, G. Liu, V. Balaram, A. Rita Lado Ribeiro, et al., Worldwide cases of water pollution by emerging contaminants: a review, Environ. Chem. Lett. 20 (2022) 2311–2338. https://doi.org/10.1007/s10311-022-01447-4.
[2] L. Malaeb, G.M. Ayoub, Reverse osmosis technology for water treatment: State of the art review, Desalination. 267 (2011) 1–8. https://doi.org/10.1016/j.desal.2010.09.001.
[3] W. Pronk, A. Ding, E. Morgenroth, N. Derlon, P. Desmond, et al., Gravity-driven membrane filtration for water and wastewater treatment: A review, Water Res. 149 (2019) 553–565. https://doi.org/10.1016/j.watres.2018.11.062.
[4] L. Gurreri, A. Tamburini, A. Cipollina, G. Micale, Electrodialysis applications in wastewater treatment for environmental protection and resources recovery: A systematic review on progress and perspectives, Membranes. 10 (2020) 146. https://doi.org/10.3390/membranes10070146.
[5] S.A. Zargar, E. Soroush, A.M. Khachatourian, M. Golmohammad, A. Nemati, Synthesis of Novel 2D/2D Ti3C2Tx MXene/1T-MoS2

Heterostructure Enhanced with Carbon Nanotubes as a Highly-Efficient Electrode for Hybrid Capacitive Deionization, J. Alloys Compd. 981 (2024) 173765. https://doi.org/10.1016/j.jallcom.2024.173765.

[6] S.I. Ali Shah, M. Anwar, I. Ullah, M. Sultan, N. Zada, J. Ali Khan, Suitable Photocatalysts and Photoelectrodes for H2 Generation via Water Splitting: A Comprehensive Review, Int. J. Hydrog. Energy. 232 (2026) 154525. https://doi.org/10.1016/j.ijhydene.2026.154525.

[7] D. An, X. Xie, K. Zhang, Recent advancement in 2D metal-free photocatalyst: structures, modification strategies and applications in water purification, J. Environ. Chem. Eng. 14 (2026) 123055. https://doi.org/10.1016/j.jece.2026.123055.

[8] S.A. Zargar, M. Gharivi, O. Bagheri, A.M. Khachatourian, A. Hashemi, Green synthesis of Z-scheme N-doped g-C3N4/Nd-doped ZnO heterostructure by pomegranate waste peel with enhanced photocatalytic performance for organic pollutants removal and antibacterial activity, FlatChem. 48 (2024) 100736. https://doi.org/10.1016/j.flatc.2024.100736.

[9] F. Amano, K. Nogami, M. Tanaka, B. Ohtani, Correlation between surface area and photocatalytic activity for acetaldehyde decomposition over bismuth tungstate particles with a hierarchical structure, Langmuir. 26 (2010) 7174–7180. https://doi.org/10.1021/la904274c.

[10] M. Khatun, P. Mitra, S. Mukherjee, Effect of band gap and particle size on photocatalytic degradation of NiSnO3 nanopowder for some conventional organic dyes, Hybrid Adv. 4 (2023) 100079. https://doi.org/10.1016/j.hybadv.2023.100079.

[11] V.V. Sre, M.K. Okla, B. Janani, M.A. Abdel-Maksoud, S.S. Al-Amri, et al., A novel sunlight driven Z scheme ZnCdS QDs deposited over g-C3N4 photocatalyst for photoinactivation of E. coli cells, J. Water Process Eng. 59 (2024) 104957. https://doi.org/10.1016/j.jwpe.2024.104957.

[12] H. Solayman, A. Abd Aziz, Y. Noor Yahya, K. Hon Leong, L.Ching Sim, et al., CQDs Embed g-C3N4 Photocatalyst in Dye Removal and Hydrogen Evolution: An Insight Review, J. Water Process Eng. 57 (2024) 104645. https://doi.org/10.1016/j.jwpe.2023.104645.

[13] Z. Wang, Y. Wei, C. Liu, Y. Teng, P. Shu, X. Peng, Rare Earth Doping-Regulated G-C3N4-Based Photocatalysts: Heterojunction Construction, Mechanisms, and Synergistic Applications in Energy and Environment, Adv. Sustain. Sys. 10 (2026) e70458. https://doi.org/10.1002/adsu.70458.

[14] M.A. Khan, S. Mutahir, I. Shaheen, Y. Qunhui, M. Bououdina, M. Humayun, Recent advances over the doped g-C3N4 in photocatalysis: A review, Coord. Chem. Rev. 522 (2025) 216227. https://doi.org/10.1016/j.ccr.2024.216227.

[15] E. Borfecchia, S. Maurelli, D. Gianolio, E. Groppo, M. Chiesa, et al., Insights into adsorption of NH3 on HKUST-1 metal–organic framework: a multitechnique approach, J. Phys. Chem. C. 116 (2012) 19839–19850. https://doi.org/10.1021/JP305756K.

[16] A. Khan, M. Le Pivert, A. Ranjbari, D. Dragoe, D. Bahena-Uribe, et al., Cu-Based MOF/TiO2 Composite Nanomaterials for Photocatalytic Hydrogen Generation and the Role of Copper, Adv. Funct. Mater. 36 (2026) 2501736. https://doi.org/10.1002/adfm.202501736.

[17] E. Soroush, S.A. Zargar, R. Ahadi Dolatsara, A. Malek Khachatourian, M. Golmohammad, Facile Fabrication of Copper-Based Metal-Organic-Framework/Graphene Hybrid Supported on Highly Stretchable Wooden Substrate for in-Plane Micro-Supercapacitor with Potential Applications as Wearable Devices, Electrochim. Acta. 521 (2025) 145905. https://doi.org/10.1016/j.electacta.2025.145905.

[18] H. Mirhosseini, T. Shamspur, A. Mostafavi, S. Dan, A. Akhtarpoor, Preparation of an Ag-loaded Cu-MOF nanocomposite with excellent activity for photocatalytic degradation of tetracycline and enhanced antibacterial activity, New J. Chem. 50 (2026) 7329–7340. https://doi.org/10.1039/d5nj04742k.

[19] S. Zhu, Q. Sun, C. Sun, Z. Zhu, J. Qu, et al., Efficient antibiotic degradation catalyzed by oxygen vacancy and Cu-Doped Cu-MOF under visible light, Sep. Purif. Technol. 347 (2024) 127377. https://doi.org/10.1016/j.seppur.2024.127377.

[20] H. Suleman Yaseen, R. Liu, L. Deng, F. UI Hassan, Y. Jiang, et al., Enhanced Charge Regulation in a Bimetallic CoFe-MOF/g-C3N4 Hybrid for Efficient Hydrogen Evolution, J. Mater. Sci. 61 (2026) 14028–14043. https://doi.org/10.1007/s10853-026-12683-2.

[21] H. Zhao, S. Wang, N. Wang, G. Wang, S. Li, et al., Oxidized g-C3N4 Assembled Cu/Co-MOF Composites for Photocatalytic Hydrogen Production and Pollutant Degradation, Mater. Today Chem. 53 (2026) 103484. https://doi.org/10.1016/j.mtchem.2026.103484.

[22] Y. Wang, Y. Yang, X. Zhang, Y. Shi, Q. Liu, K. Wu, Boosting Photocatalysis: Cu-MOF Functionalized with g-C3N4 QDs for High-Efficiency Degradation of Congo Red, Catalysts. 15 (2025) 1169. https://doi.org/10.3390/catal15121169.

[23] A. Panchakeaw, S. Nonthing, R. Dulyasucharit, S. Nanan, Improved photocatalytic activity of magnetically separable Fe3O4/ZnO photocatalyst for complete sunlight-active removal of tetracycline antibiotic, Chem. Phys. Lett. 862 (2025) 141868. https://doi.org/10.1016/j.cplett.2025.141868.

[24] A. Moeini, I. Khezri, R. Ahadi Dolatsara, M. Hajiebrahimi, H. Beydaghi, et al., Fe3O4-based magnetic nanoparticles for the removal of water contaminants, Dalton Transact. 55 (2026) 2361–2399. https://doi.org/10.1039/d5dt02011e.

[25] S. Nonthing, A. Panchakeaw, R. Dulyasucharit, H. Nakajima, S. Nanan, Fe3O4/BiOCl Photocatalyst with Magnetic Recovery Property for Solar-Light-Responsive Removal of Rhodamine B Dye, OpenNano. 26 (2025) 100260. https://doi.org/10.1016/j.onano.2025.100260.

[26] A. Moeini, A. Ghiasi, M. Dehghani Mohammad Abadi, A. Malek Khachatourian, H.R. Madaah Hosseini, M. Malek, Zn-Doped Superparamagnetic Iron Oxide Nanoparticles–LCysteine Functionalized@ N-Doped Graphene Quantum Dots as Multifunctional Contrast agents for Dual-Model Imaging (MRI & FI), Mater. Des. 256 (2025) 114269. https://doi.org/10.1016/j.matdes.2025.114269.

[27] A. Taravati, A. Poursattar Marjani, S. Bibak, H. Sarreshtehdar Aslaheh, One-Pot Synthesized g-C3N4/Fe3O4/CuO Magnetic Photocatalyst for One-Pot Synthesis of 2-Amino-4 H-Benzochromenes and Methylene Blue Photodegradation, Sci. Rep. 15 (2025) 36817. https://doi.org/10.1038/s41598-025-23196-4.

[28] Z. Zhu, Z. Lu, D. Wang, X. Tang, Y. Yan, et al., Construction of high-dispersed Ag/Fe3O4/g-C3N4 photocatalyst by selective photo-deposition and improved photocatalytic activity, Appl. Catal. B: Environ. 182 (2016) 115–122. https://doi.org/10.1016/j.apcatb.2015.09.029.

[29] Z. Zhang, X. Li, H. Chen, G. Shao, R. Zhang, H. Lu, Synthesis and properties of Ag/ZnO/g-C3N4 ternary micro/nano composites by microwave-assisted method, Mater. Res. Express. 5 (2018) 015021. https://doi.org/10.1088/2053-1591/aaa1dc.

[30] H. Rahbari, R.A. Dolatsara, A. Moeini, S.A. Zargar, A. Shahraki, et al., Ambient-Air Fabrication of Triple-Cation Mixed-Halide Perovskite Cells with High-Speed Doctor-Blade Printing by PEG as Ink Additive and Triton X-100 as ETL Surface Modifier, ACS Appl. Electron. Mater. 7 (2025) 964–982. https://doi.org/10.1021/acsaelm.4c01518.

[31] Z. Abdi, S.A. Zargar, O. Bagheri, R.A. Dolatsara, A.M. Khachatourian, Preparation of Rod-Like Ni-doped ZnO Anchored onto N-Doped Graphene Nanosheets for Pharmaceutical Pollutant Removal and Evaluation of Phytotoxicity, Mater. Sci. Semicond. Process. 188 (2025) 109205. https://doi.org/10.1016/j.mssp.2024.109205.

[32] F. Ramezani Araghi, M. Gharivi, A. Moeini, S.A. Zargar, A. Malek Khachatourian, Y.-S. Borghei, Phase-Engineered 1T-MoS2-Silk Fibroin Nanohybrid for Efficient Photothermal Cancer Therapy,

Mater. Today Commun. 54 (2026) 115442. https://doi.org/10.1016/j.mtcomm.2026.115442.

[33] F. Sousani, S.K. Sadrnezhaad, P. Abachi, H. Mahtabpour, Ni0.8Co0.2/Zn0.8Cd0.2S/g-C3N4 Ternary Nano-Photocatalyst for Improved Visible-Light-Driven Photocatalytic H2 Evolution and Pollutants Degradation, Int. J. Hydrog. Energy. 51 (2024) 281–299. https://doi.org/10.1016/j.ijhydene.2023.10.001.

[34] Z.L. Wu, C.H. Wang, B. Zhao, J. Dong, F. Lu, et al., A semi-conductive copper−organic framework with two types of photocatalytic activity, Angew. Chem. Int. Ed. 55 (2016) 4938−4942. https://doi.org/10.1002/anie.201508325.

[35] H. Yousefi, S.R. Shabanian, G. Dashtpeyma, J. Ahmadpour, Fabrication of Bio-Compatible BiOI/Hydroxyapatite/g-C3N4 Ternary Photocatalyst with Enhanced Charge Separation for Oxidative Desulfurization of Fuels under Visible Light, Fuel. 406 (2026) 136901. https://doi.org/10.1016/j.fuel.2025.136901.